Research Article | Vol. 12, No. 6 / 1 Jun 2022 / *Optical Materials Express* 2382

Optical Materials EXPRESS

Bandgap engineering, monolithic growth, and operation parameters of GaSb-based SESAMs in the 2–2.4 µm range

B. ÖZGÜR ALAYDIN,[1,2,3] MARCO GAULKE,[1,3,*] JONAS HEIDRICH,[1] MATTHIAS GOLLING,[1] AJANTA BARH,[1] AND URSULA KELLER[1]

[1] *ETH Zurich, Department of Physics, Institute for Quantum Electronics, Auguste-Piccard-Hof 1, Zurich 8093, Switzerland*
[2] *Current address: Sivas Cumhuriyet University, Department of Physics, Turkey*
[3] *The authors contributed equally*
[*] *gaulkem@ethz.ch*

Abstract: We present the detailed growth and characterization of novel GaSb-based semiconductor saturable absorber mirrors (SESAMs) operating in the 2–2.4 µm spectral range. These SESAMs at different wavelengths are bandgap engineered using ternary material compositions and without strain compensation. We observe that even when the thickness of quantum wells (QWs) exceeds the critical thickness we obtain strain relaxed SESAMs that do not substantially increase nonsaturable losses. SESAMs have been fabricated using molecular beam epitaxy with a $AlAs_{0.08}Sb_{0.92}$/GaSb distributed Bragg reflector (DBR) and strained type-I $In_xGa_{1-x}Sb$ or type-II W-like AlSb/InAs/GaSb QWs in the absorber region. All the type-I SESAMs show excellent performance, which is suitable for modelocking of diode-pumped semiconductor, ion-doped solid-state, and thin-disk lasers. The recovery time of the type-II SESAM is too long which can be interesting for laser applications. The dependence of the SESAM design, based on its QW number, barrier material, and operation wavelength are investigated. A detailed characterization is conducted to draw conclusions from macroscopic nonlinear and transient absorption properties at different wavelengths in the 2–2.4 µm range for the corresponding devices.

1. Introduction

Ultrafast lasers have a high impact on many applications in science. Industrial applications greatly benefit from progress in passively modelocked diode-pumped solid-state lasers for which the semiconductor saturable absorber mirror (SESAM) [1] solved the long-lasting Q-switching instability problem [2]. Most of these lasers operate in the near infrared (near-IR) regime typically using GaAs and InGaAs quantum well (QW) SESAMs and the performance was pushed in many key dimensions in terms of shorter pulses [3], more power [4] and higher repetition rates [5,6] in many cases by orders of magnitude. Until recently there have been only a few results reported for SESAM modelocked lasers operating in short-wave infrared (SWIR) spectral range even though there is a strong interest for many applications [7–11]. The performance of many of these lasers however was limited by the quality of the available SWIR SESAMs. The first SESAMs grown on GaSb substrates have been reported 17 years ago [12] for type-II and 13 years ago for type-I QWs [13]. Even though their dependence of recovery dynamics on growth temperature and QW position has been investigated [14,15], no complete set of saturation parameters have been directly measured until recently [16]. Also, the maximum absorber wavelength for type-I quantum wells reported is to the best of our knowledge 2.05 µm even when lattice-relaxed quaternary InGaAsSb QWs are used with negligible strain [17].

#459232
Journal © 2022

https://doi.org/10.1364/OME.459232
Received 1 Apr 2022; accepted 16 May 2022; published 1 Jun 2022

In the near-IR regime, the GaAs-based SESAMs with absorber layers grown at normal temperatures (580 °C) with high crystalline quality, the recovery time is in the order of hundreds of picoseconds to nanoseconds. However, for fast saturable absorber-based modelocking picoseconds and for soliton modelocking with dispersion compensation a few tens of picoseconds recovery times are typically required [18]. Therefore, additional defects have been introduced into and around the absorber layers to obtain a SESAM with shorter recovery time via recombination over nonradiative defect trapping. Such defect engineering for fast SESAMs was obtained with low-temperature (LT) MBE growth [19,20], ion-implantation [21,22], placing absorber QWs or quantum dots next to LT grown AlAs barriers [23], or placing absorber layers close to the SESAM chip surface (with the trade-off of lower damage fluences [24]). The damage threshold can be increased significantly by placing the semiconductor air interface into the node of the standing wave [24]. Generally, a more careful balance between fast recovery times and low nonsaturable losses has to be obtained [20]. For LT-grown fast GaAs-based saturable absorbers it was shown that As antisite defects are mostly neutral and only about 10% are ionized [25]. However, the neutral As antisites substantially reduce the modulation depth and increase the nonsaturable losses [26]. Neutral As antisites and therefore the nonsaturable losses can be reduced with additional annealing after the MBE growth forming arsenic precipitates [26] and with additional Be-doping [27]. On the other hand, LT-grown InGaAs/AlAs QW saturable absorbers benefit from defects in AlAs that are rather fixed at their positions and cannot easily be moved by annealing. More recently another approach was demonstrated with quantum dot SESAMs operating at a wavelength around 1 µm which resulted in fast recovery without defect engineering using normal growth temperatures for high crystalline quality [28].

In contrast, for 2-µm GaSb-based type-I QW SESAMs no defect engineering is required to obtain a fast SESAM because of enhanced Auger recombination [17]. This is clearly a benefit of this material for saturable absorber applications. Pajaeste et al. [17] also showed that LT growth of such SESAMs did not significantly affect the recovery dynamics even though additional defects were introduced in LT-grown GaSb-based materials. They found that the carriers more likely recombined via a conduction band Auger process as long as both the electrons and holes are well localized within the QWs with negligible thermally induced delocalization. This results in a shorter recovery time for the SESAM due to nonradiative Auger recombination which dominates in semiconductors with a low bandgap energy, such as GaSb-based materials [29]. The high excitation levels in fully saturated SESAMs further helps in this case because the probability for such Auger recombination scales with n^2p if two electrons are involved, where n is the electron density and p is the hole density. For undoped materials (i.e., $n = p$) this results in an Auger recombination rate proportional to n^3. Further investigations concluded that crystal strain (tensile and compressive) did not have a significant effect on the recovery dynamics [15]. In this paper, we show that strain relaxed SESAMs do not significantly increase nonsaturable losses and still work well for modelocking. In prior work no complete optical characterization of the macroscopic SESAM parameters was performed. Even though the QW materials have been used in emitting devices up to 2.8 µm [30,31], no bandgap engineering of absorbers has been published over the wavelength range from 2–2.4 µm for type-I QW saturable absorbers so far.

In [16] we explained how we can measure the macroscopic SESAM parameters, such as the modulation depth ΔR, nonsaturable losses ΔR_{ns}, saturation fluence F_{sat}, rollover fluence F_2 and recovery dynamics in a wavelength regime from 1.9 to 3 µm with a high accuracy (<0.04%) over a wide fluence range (0.1–1500 µJ/cm^2) with very similar performance as demonstrated before with near-IR SESAMs [32].

Here, we give a comprehensive description and discussion of the molecular beam epitaxy (MBE) growth and design parameters using both type-I and type-II band alignments in GaSb-based SESAMs and put them in perspective to their macroscopic SESAM parameters for an operation wavelength from 2–2.4 µm for the first time to the best of our knowledge. For

Optical Materials EXPRESS

long-wavelength GaSb-based SESAMs we can confirm the expectation that high crystal quality of undoped MBE growth results in low nonsaturable losses [20]. In this paper we present several GaSb-based SESAM designs with the operation from 2–2.4 µm, ideally suited for passively modelocked diode-pumped Cr:ZnS lasers at a center wavelength of around 2.4 µm [11,33] and vertical external-cavity surface-emitting lasers (VECSELs) [34] at a center wavelength of around 2 µm [35].

For these lasers we typically require fast SESAMs with a recovery time less than ≈10 ps and with up to a few percent modulation depth, low saturation fluences and nonsaturable losses much lower than the modulation depth. For the SWIR wavelength regime, a highly reflective distributed Bragg reflector (DBR) has still a reasonable thickness for heat transfer, we therefore choose monolithic growth to keep nonsaturable losses small and fabrication simple. The designed SESAMs benefit from good electron and hole localization to achieve a high Auger recombination rate. Type-I InGaSb SESAMs for an increasing operation wavelength have increased strain due to a higher In content and an increased thickness of QW layers, which leads to a strain-relaxed SESAM at 2.35 µm. In comparison we also present a low-strain type-II AlSb/InAs/GaSb W-like multi-QW SESAM at 2.35 µm wavelength. We also vary the number of QWs and their barrier material. The structural quality of SESAMs is determined by x-ray diffraction analysis, cross-section scanning electron microscope (SEM) and optical microscope images. The operating wavelengths of SESAMs are determined with linear reflectivity and photoluminescence (PL) measurements. All the modelocking-relevant macroscopic SESAM parameters are determined from recovery dynamics and nonlinear reflectance properties which are measured using a newly installed optical characterization infrastructure for the SWIR and mid-IR wavelength regime at ETH Zurich.

2. Material and methods

Growth is performed in a Veeco Gen III MBE. An Sb cracker with the bulk at 540 to 570 °C and the cracking zone at 900 °C is used to crack the Sb_4 molecules to Sb_2. The As/Sb ratio is carefully adjusted to obtain the lattice matched ternary material $AlAs_{0.08}Sb_{0.92}$. The substrate is a 2″ (001)-oriented, n-type, single-side polished GaSb wafer with a thickness of 500 µm from Wafer Technology Ltd. Growth is performed in normal order (i.e., right-side up) starting with the highly reflective DBR using 20-24 high- and low-index layer pairs and an absorber region on top. Prior to growth the wafers are heated with thermocouples temperature-controlled heaters. The surface temperature is calibrated using the transition of the high-energy electron diffraction (RHEED) pattern from 2×5 to 1×3 which happens around 385-390 °C [36,37]. To prevent surface degradation, Sb counter pressure is started during heat-up around 350 °C. Deoxidation of the substrate is done at 550 °C for 15 minutes. A clear RHEED signal belonging to the 1×3 pattern is obtained after deoxidation. Substrate temperature for the mirror growth is 520 °C, the absorber region is grown at 480 °C. The higher substrate temperature leads to lower defect densities, but the temperature decrease is necessary to prevent indium (In) re-evaporation and diffusion from the QWs.

In addition to SESAMs, we are investigating growth conditions for optically pumped VECSELs [38]. For increased heat extraction capabilities, these devices are grown in reverse order (i.e., upside down) and are then flip-chip bonded before substrate removal. We are therefore in the process of adapting our mirror growth conditions to lower growth temperatures to maintain the quality of the QWs during the long annealing time of the DBR growth. This is clearly not ideal in terms of defect density. However, we hope to achieve superior thermal properties by using substrate removal techniques on SESAMs and VECSELs in the near future.

After growth, the Sb was switched off around 350 °C while cooling down to have a smooth surface. For the 2.05-µm SESAMs, the flux values during growth are $1.7 \cdot 10^{-7}$, $2.7 \cdot 10^{-7}$ and $1.3 \cdot 10^{-7}$ torr for In, gallium (Ga), and aluminum (Al), respectively. These fluxes result in growth

Optical Materials EXPRESS

rates in the range of 1100 nm/h for GaSb and 900 nm/h for $AlAs_{0.08}Sb_{0.92}$. The ratio of group V (As, Sb) to group III (Al, Ga, In) is approximately 2 for InGaSb. For 2.35-µm SESAMs, the growth rates were reduced to 700 nm/h for GaSb and 600 nm/h for $AlAs_{0.08}Sb_{0.92}$. The ratio of group V flow for the InGaSb QWs of these SESAMs is approximately 3.8. For the type-II QWs antimony soaking after each arsenic-containing layer is done for 3 seconds to have a smoother interface after each layer and to control the strain [39]. A smooth interface is essential for good carrier recombination.

3. Results and discussion

The designed and measured SESAM parameters are summarized in Table 1 and were determined by the measurements described in more detail in the following. For clarity, only measurements for SESAM 3 and sometimes additionally for SESAM 1 and 6 are shown indicated in each figure, however the result of each measurement can be found in the summarizing Table 1.

Table 1. Overview of SESAM parameters. This table summarizes the SESAM parameters from the design or obtained via different linear and nonlinear measurements from 2.05-2.35 µm. The first wavelength λ is determined by PL or linear reflection whereas the second λ_{Fsat} is the probe wavelength for the SESAM used during characterization. A is the pump-probe, bi-exponential weighting of equation (1).”

No.	Type	QW#	d_{QW} / nm	In content / %	λ / µm	A	τ_1 /ps	τ_2 / ps	λ_{Fsat} / µm	F_{sat}/µJ cm^{-2}	ΔR / %	ΔR_{ns} / %	F_2/mJ cm^{-2}
1	I	3	11.5	26	2.06	0.7	0.7	32	2.05	2.9	1.8	0.15	51
2	I	3	14.5	33	2.26	0.6	0.2	1.8	2.25	5.0	1.1	0.1	35
3	I	3	16	33	2.35	>0.9	0.1	<1	2.35	12	1.5	0.4	32
4	I	3	16	33	2.35	0.8	0.1	9.3	2.35	11	1.5	0.12	50
5	I	1	16	33	2.35	>0.9	0.1	<1	2.35	21	0.5	0.14	37
6	II	20	12.5	-	2.32	0.5	0.26	>5000	2.35	3.1	4.8	0.5	30

In Fig. 1 the two QW configurations (type-I and type-II) compared in this work are illustrated. The band edges and wave functions are calculated using nextnano++, a commercial software with an eight-band k.p model [40]. Fig. 1(a) shows a type-I configuration, where a potential well for holes and electrons exist in same material layer, whereas in Fig. 1(b) a type-II configuration is shown having spatially separate wells for electrons and holes. In type-I QWs electron and hole wave functions show maximum overlap in the same layer, whereas a more complex wave function overlap is observed in type-II QWs. However, we can demonstrate that for the type-II configuration the wave function overlap is still sufficient for saturable absorption with significant modulation depth and low nonsaturable loss by simply increasing the number of type-II QWs (Table 1). However, because the wave function overlap integral and therefore the absorption strength in type-II QWs is lower compared to a type-I QW we observe a much longer relaxation time of more than 5 ns (Table 1). This can be explained by the much lower Auger recombination in type-II QWs which becomes advantageous for example in active devices, such as interband cascade lasers [41] or VECSELs. However, this makes type-II SWIR SESAMs not fast and therefore not useful for passive modelocking. Indeed, we have seen limited stability with soliton modelocked Cr:ZnS lasers at 250 MHz pulse repetition rates [11] and we achieved no stable modelocking at a pulse repetition rate of 2 GHz [33].

In Fig. 2 the SESAM designs investigated in this work are compared. The absorption properties of SESAMs can be tuned by changing the QW number and their position against the standing-wave pattern of the reflected laser beam inside the SESAM device (see red lines in Fig. 2). The close to 100% reflectivity with small nonsaturable losses results in a standing wave pattern with well-defined nodes (i.e., intensity close to zero) and antinodes with a relative intensity of about

Optical Materials EXPRESS

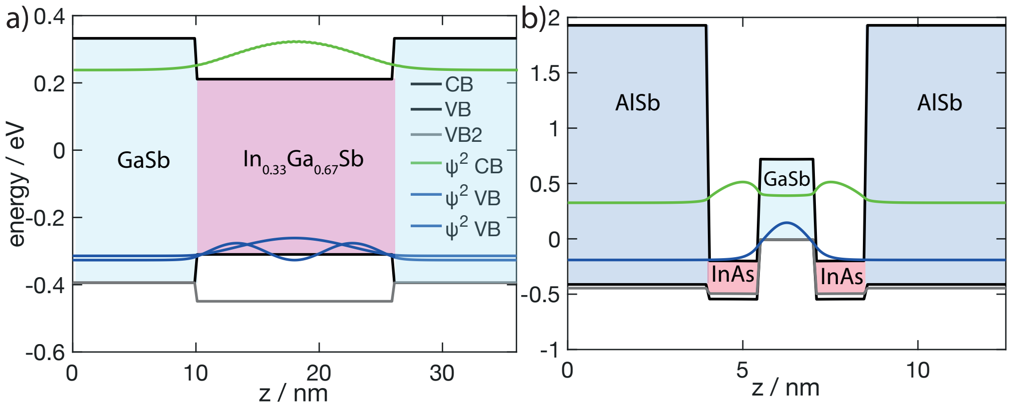

Fig. 1. Band alignments and the corresponding absolute squared quantum mechanical wave functions used for SESAMs in this work. Panel a) shows a ternary strained InGaSb QW embedded in GaSb which has a type-I configuration used in SESAM 1-5. In b) a type-II W-type QW configuration is shown which is used for SESAM 6. CB: conduction band, VB: valance band.

0.27 in comparison to the normalized peak intensity of 4 for a 100% reflector. The relative intensity is also referred to as the field intensity enhancement $\xi(z) \propto |E(z)|^2$ [1,4142], where z is the distance from the SESAM substrate perpendicular to the QW layers and along the MBE growth direction, $E(z)$ is the standing wave electric field due to the reflected laser beam. For all cases we choose an antiresonant design with a node in the standing wave at the air interface to obtain high damage threshold. Within this study we want to obtain low saturation fluence with negligible and flat group delay dispersion (GDD) which is achieved for such an antiresonant design with the QW absorbers placed at the antinodes [42]. To study the effect of QW number and crystal strain relaxation on absorption properties, we have designed a set of SESAMs for wavelengths of 2.05-2.35 µm (Fig. 2(a)-(e)). In addition, as a reference we have also designed a type-II QW SESAM at the longest wavelength of 2.35 µm (Fig. 2(f)).

All antiresonant SESAMs have the QWs arranged around an antinode of the electric field which corresponds to the traditional antiresonant low-finesse design introduced in the near infrared regime [1,42]. From SESAM 1 to SESAM 3 the design wavelength is increased from 2.06 µm, to 2.26 µm and finally 2.35 µm, resulting in an increasing thickness of the 20-pair GaSb/$AlAs_{0.08}Sb_{0.92}$ DBR from 5.8 µm to finally 6.7 µm. In the absorber section, both the In content and the thickness of the QW layers are increased accordingly (Table 1). For the 2.35-µm SESAM 4 the barrier material has been changed from GaSb to $AlAs_{0.08}Sb_{0.92}$ in order to investigate its influence on the SESAM parameters. The In flux was adjusted to keep the design wavelength constant. For the 2.35-µm SESAM 5 the QW number is reduced from 3 to 1 to experimentally verify the predicted saturation parameter scaling and confirm the reliability of our design recipe. The 2.3-µm SESAM 6 uses the type-II configurations of Fig. 1(b) having 20 W-type QWs arranged around an antinode of the standing wave. For this investigation we keep the maximum field enhancement constant because no topcoatings have been applied which can give an additional design parameter for lower inverse saturable absorption and higher damage threshold [24].

Fig. 3 demonstrates the growth quality achieved for the investigated 2.35-µm SESAM 3 in a-d) and compares it to 2.06-µm SESAM 1 (Fig. 3(e)) and 2.3-µm type-II SESAM 6 (Fig. 3(f)). In Fig. 3(a) we observe an optically smooth surface in the Nomarski microscope image. This should give close to zero scattering losses which is indispensable when used as an intracavity element. Fig. 3(b) shows the dark field microscopy image. Here we can see few defects lighting up as white

Optical Materials EXPRESS

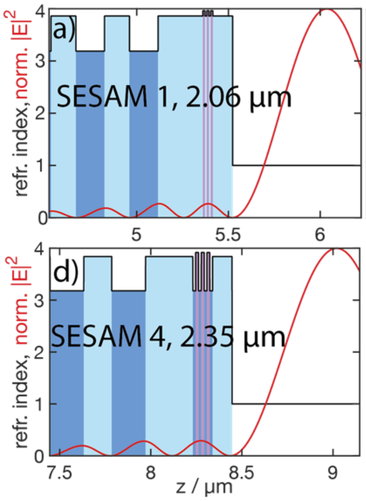

Fig. 2. SESAM designs: a)-f) show the design of SESAM 1-6, respectively. GaSb is marked in light blue whereas $AlAs_{0.08}Sb_{0.92}$ is shown in dark blue. $In_xGa_{1-x}Sb$ QWs are shown in pink. The normalized electric field intensity is shown in red. All SESAM are designed antiresonant with a node of the electric field at the semiconductor air interface. The QWs are always placed around the antinode of the electric field to increase the interaction. SESAM 1-3 gradually shift the wavelength from 2.05 to 2.35 µm. SESAM 4 changes the barrier material from GaSb to $AlAs_{0.08}Sb_{0.92}$ and SESAM 5 reduces the QW number to 1. SESAM 6 uses a type-II configuration and 20 QWs.

dots. The defect density is low even though the growth has been done at LT (480 °C). Fig. 3(c) shows a cross-section SEM image. This allows for investigation of actual layer thicknesses, which in our case matches the design. The interfaces are clearly visible and the layers are separated by straight lines in the DBR. Even the QWs could be resolved as shown in the zoomed in version in Fig. 3(c). As the QW layers are strained due to lattice mismatch with $\frac{\Delta a}{a} = 2.1\%$ their interfaces do not have the same quality. However, as their interface roughness is below the optically relevant length scales, it does not introduce any significant scattering losses. Fig. 3(d) shows the XRD measurement of the 2.35-µm SESAM 3. These measurements are used to determine the In concentration via fit and also give an insight in the layer thicknesses and their periodicity. The lattice mismatch for InAs/AlSb is $\frac{\Delta a}{a} = -0.62\%/0.65\%$ respectively. Next to the highest substrate peak a broad side peak is observed which comes from the compressively strained QWs. However, the absence of any distinct features like they are visible in Fig. 3(e) or Fig. 3(f) suggests that the structure is strain relaxed. This is not surprising since the total thickness of the QWs at this high In concentration exceeds the critical thickness as shown previously [43]. Even though Fig. 3(e) shows a strained QW they do not relax since the In concentration and QW thickness for the 2.06-µm SESAM 1 are substantially lower and do not cross the critical limit. The narrow peaks in Fig. 3(f) for the type-II SESAM 6 indicate a high crystalline and growth quality.

From the XRD fit, we have estimated the type-II QW layer thicknesses as 4 nm, 1.45 nm, and 1.55 nm for AlSb, InAs, and GaSb, respectively. In addition, the fact that the 0^{th} satellite peak (second highest peak in Fig. 3(f)) is shifted to the left of the GaSb substrate peak (highest peak in Fig. 3(f)), indicates that there is a small compressive strain in the structure.

Even though monolithically grown ternary material-based type-I SESAMs seem to strain relax after a certain wavelength, it still maintains the good SESAM parameters (Table 1) with good surface quality and negligible scattering losses. In fact, we successfully demonstrated

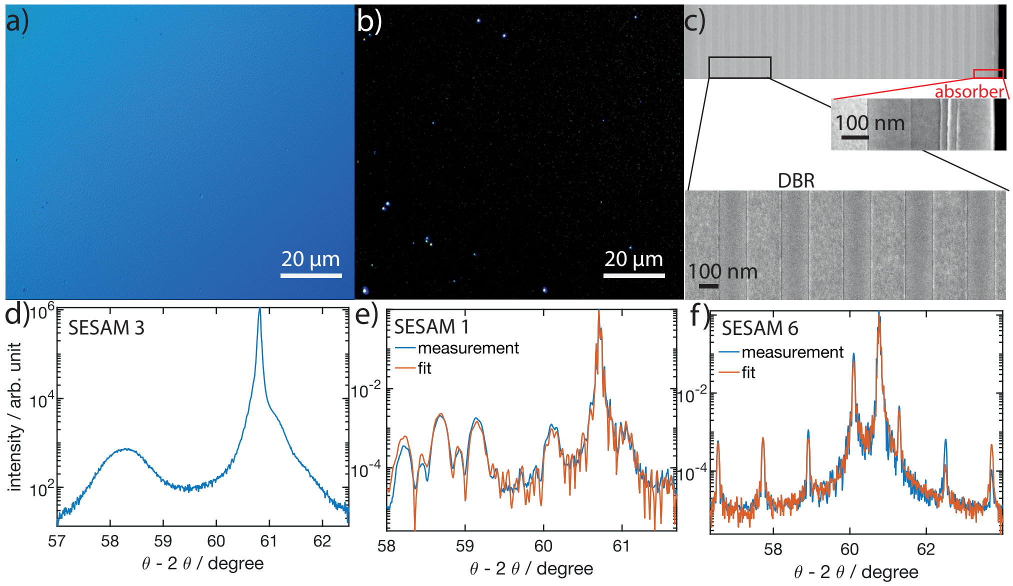

Fig. 3. Growth quality analysis. In a)/b) the Nomarski/dark field microscope images of 2.35-µm SESAM 3 are shown. The surface is optically smooth with very few defects which appear as white dots in the dark field image. In c) a cross section SEM of the 2.35-µm SESAM 3 shows an overview of the structure and zoomed in images of the DBR (black) and the absorber region (red). Clear interfaces are visible in both the cases. In d) the XRD analysis of SESAM 3 is shown. Compared to the XRD analysis of 2.06-µm SESAM 1 (e)) and 2.3-µm type-II SESAM 6 (f)) much less distinct features are visible which indicates strain relaxation in SESAM 3.

a high-power and femtosecond Cr:ZnS solid-state laser modelocked with the strain relaxed SESAMs using 3-5% output couplers [11,33].

Figure 4 summarizes the optical characterization performed on the SESAMs illustrating linear and nonlinear reflectance as well as the transient time response. A detailed description of the measurement setups and the methods to derive the SESAM parameters are given in [16]. Fig. 4(a) shows the linear spectral reflectance measurements for the 2.06-µm SESAM 1 (S1) and the 2.35-µm SESAM 3 (S3). The measurements are obtained by a Bruker Vertex 80v FTIR with an additional PL module. One can see that the high reflecting region of the DBR (i.e., stopband) is shifted as intended in the design. To locate the intrinsic wavelength of a QW, PL measurement is a standard method [12], however, it is not necessary for a SESAM device since the nonradiative recombination channels are sufficient for an absorber. The PL peak for SESAM 1 is detected at 2.06 µm, which is 300 times lower than the PL originating from GaSb substrate at 1.7 µm (not shown here) due to dominant nonradiative recombination of carriers in the QWs. While SESAM 1 still exhibits a PL signal, SESAM 3 does not show any PL as the strength of nonradiative recombination mechanisms are increased and apparently dominated by Auger enhanced trap state trap state recombination [29]. In the absence of PL, we use the absorption edge visible in the stopband to find the absorber's operation wavelength.

Figure 4(b) reveals the saturation properties of the 2.35-µm SESAM 3 at a fixed test wavelength. Measurements are carried out around the absorber's wavelength previously determined from PL and/or reflectance. In this case the reflectance is measured as a function of incident fluence (i.e., pulse energy per area) at a fixed wavelength and has been performed for all the investigated SESAMs. The SESAM parameters, extracted by the fit as described in [16], are given in

Optical Materials EXPRESS

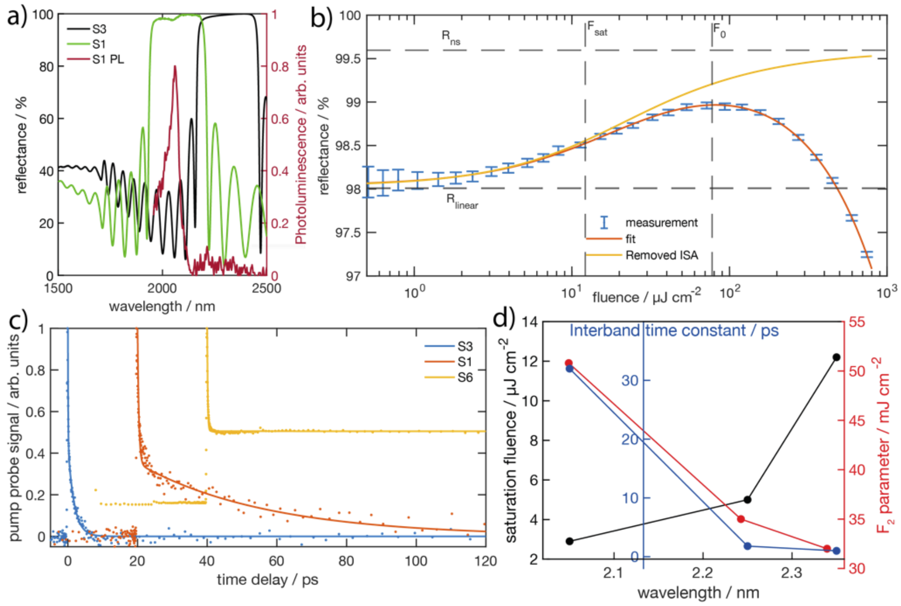

Fig. 4. Optical characterization. a) shows the spectral reflectance measurements and the corresponding PL of the 2.06-µm SESAM 1 (S1) and reflectance of 2.35-µm SESAM 3 (S3) as marked in the legend. S3 does not show a PL signal. In b) nonlinear reflectance measurement of S3 (blue) is shown with a fit (red) performed to extract the SESAM parameters. Yellow line represents the fit without considering the ISA. c) shows the transient dynamics measurements of SESAM 3, 1 and 6 shifted by a 20-ps step each in x-axis direction for clarity. Recovery time of S3 barely shows any slower component. The 2.3-µm type-II SESAM 6 (S6) is too slow for good passive modelocking application. The measurements (dots) are fitted with corresponding bi-exponential functions (solid). d) shows the wavelength dependence of 3-QW type-I SESAMs with comparable designs (SESAM 1-3). With increasing wavelength, the saturation fluence increases, the SESAMs become faster, and the rollover happens at lower fluences.

Table 1. Starting at the linear reflectance R_{linear} at low incident fluences the reflectance increases when the saturation fluence (F_{sat}) is reached, increasing further until reaching the nonsaturable reflectance (see yellow line). This level stays below 100% because of any residual scattering losses, the difference to 100% is typically referred to as the nonsaturable losses ΔR_{ns}. The maximum reflectivity is obtained at a fluence $F_0 = \sqrt{F_2 F_{sat} \Delta R}$ which becomes smaller for shorter pulses and/or higher fluences due to onset of higher order absorption effects such as two-photon absorption (TPA) leading to an inverse saturable absorption (ISA). The slope of this ISA is referred to as the rollover parameter denoted by F_2 [44].

In Fig. 4(c) the typical time-dependent responses are plotted, measured using our pump-probe setup as described in [16]. Following the modelocked intracavity lasing condition, the pump fluence is set to F_0 for the 2.06-µm SESAM 1, whereas due of restrictions in our setup, we were only able to achieve up to 2 times the F_{sat} (22 µJ/cm^2) for the SESAMs at longer wavelengths. During the investigation we however could confirm that the time constants only marginally changed when changing the pump fluence from F_{sat} to F_0. The fluence of the probe beam is set to 500/100 times lower than the pump fluence for 2.06-/2.35-µm devices respectively to prevent any saturation effects on the SESAM. The bi-exponential fit function used to fit the data is given by

$$\Delta R(\tau) = A e^{-\tau/\tau_1} + (1 - A) e^{-\tau/\tau_2} \ . \tag{1}$$

The 2.06-µm SESAM 3 exhibits a significant amount of Auger recombination and therefore the recovery time is fast, even the slower interband recombination time τ_2 (Table 1) happens within a few ps. In case of the 2.06-µm SESAM 1 the interband time constant τ_2 is in the order of 30 ps (Table 1). In contrast to these type-I SESAMs, type-II SESAM 6 shows an extremely long interband recovery which is currently limited by the repetition rate of our pump-probe light source. This means that there is still some excitation left after the inverse repetition rate of our pump-probe source which is 12.5 ns. This confirms the much lower Auger recombination rates for a type-II QWs which will become beneficial for long-wavelength VECSEL designs. The nanosecond recovery time is too slow to effectively stabilize soliton modelocking as shown with a SESAM modelocked Cr:ZnS laser [11]. Additional measures would have to be taken to reduce the recovery time to a few tens of picoseconds.

When comparing the time constants in Table 1 we can see that the barrier material around the QWs has an effect on the interband time constants (τ_2). In comparison to the 2.35-µm SESAM 3 with the barrier material GaSb, the time constant of 2.35-µm SESAM 4 with barrier material $AlAs_{08}Sb_{92}$ increases by at least a factor of 10 to 9.3 ps. This is surprising since in this deeper QW we expected a better localization of the wave functions and therefore an increased Auger-recombination. However, this observation can be used for a better self-starting of modelocking since a longer time constant up to around 10 ps can be beneficial [18,45].

When comparing the 2.35-µm SESAM 3 and 5 we can see that the number of QWs does not have a measurable effect on the time constants. This is as expected since the wave function in Fig. 1(a) does not penetrate a lot in the barrier layer and therefore no coupling of the QWs is expected.

Figure 4(d) shows the wavelength dependent SESAM parameters for the 3-QW SESAMs 1-3 having GaSb barriers investigated in this work. While the saturation fluence increases with the wavelength both the interband time constant and F_2 decreases. The decrease of the time constant is due to the higher Auger-recombination which starts to dominate at longer wavelengths. No PL signal can be observed and the time constants weakly depend on growth temperature and therefore defect density [15]. The defect related Shockley-Read-Hall recombination has minor contributions for these cases. Thus, the sufficiently fast Auger processes in the low bandgap AlGaAsSb materials help to overcome the tradeoff between the low nonsaturable losses and a fast absorber recovery for the low-temperature grown near-infrared SESAMs. The decrease in F_2 parameter most probably comes from the thicker barrier layers and the thicker GaSb/ $AlAs_{0.08}Sb_{0.92}$ DBR structure, as the TPA coefficient is pretty high for GaSb. This could be improved by using quaternary materials with smaller TPA coefficients and $AlAs_{0.08}Sb_{0.92}$ containing barrier materials. This is supported by the fact that 2.35-µm SESAM 4 has an increased F_2 parameter because some of the GaSb barrier material is replaced by $AlAs_{0.08}Sb_{0.92}$.

The increase in the F_{sat} value when going from the 2.06-µm SESAM 1 to the 2.35-µm SESAM 3 can be explained by the increasing width and depth of the QWs which increases the density of states and therefore the number of states that need to be excited to bleach the SESAM.

Even though these changes are significant all the type-I SESAM parameters are still within a good range for soliton-modelocked diode-pumped solid-state lasers, as shown at 2 µm with Ho:YAG [46] and at 2.35 µm with Cr:ZnS [11,33]. This is not surprising because for soliton modelocking the SESAM only needs to stabilize and start the modelocking. This strongly reduces the SESAM parameter requirements which becomes less effective at higher pulse repetition rates and for SESAM-modelocked VECSELs. The modulation depth (ΔR) roughly scales with the number of QWs as can be seen in Table 1 comparing SESAM 3 and SESAM 5. While the F_{sat} parameter increases, the ΔR is lowered however not enough to keep the product $F_{sat}\Delta R$ constant. The $F_{sat}\Delta R$ product is approximately given by a material constant $n_{tr}\hbar\omega$, where n_{tr} is the two-dimensional transparency density in units of cm^{-2}, and $\hbar\omega$ is photon energy [24,32]. Increasing the number of identical QWs increases ΔR and therefore to maintain the equality F_{sat}

decreases. However, this simple $F_{sat}\Delta R$ scaling with the number of QWs does not fully apply for the strain relaxed SESAMs because we expect different levels of gradual strain relaxation with different number of QWs and therefore n_{tr} is different in each case. Moreover, the concept of the transparency density reaches its limit when a SESAM is measured with femtosecond pulses since this concept relies on quasi-Fermi levels of carriers. As can be seen from the pump probe measurements with $A \approx 1$ a lot of the modulation depth appears to originate from unthermalized carriers.

Generally, the ratio $\Delta R_{ns}/\Delta R$ is better for higher crystal-quality without significant strain relaxation which can be seen for SESAM 1, 2, 6 with a ratio of around 0.1. In the case of SESAM 3, 4, 5, the SESAM 4 shows a small ratio in that range probably because of less scattering in the $AlAs_{0.08}Sb_{0.92}$ barriers in comparison to the GaSb barriers in other two. One could argue that the interface quality of $AlAs_{0.08}Sb_{0.92}$ with the InGaSb QW is better compared to GaSb which also explains the higher time constants.

We can summarize that even for strain-relaxed SESAMs at longer wavelengths where the crystalline quality declines, the microscope images do not indicate any severe degradation of the SESAMs, such as strain lines or a non-uniform surface. Also, the cross-section SEM images indicate a partial relaxation of only the QW region and any microcracks that occurred due to relaxation did not penetrate to the DBR section underneath. Moreover, nonsaturable losses are still much smaller than the modulation depth, and therefore the devices are suitable for modelocking of not only ion-doped solid-state but also semiconductor disk lasers, also referred to as VECSELs.

4. Conclusion & outlook

We have presented for the first time a detailed study on all relevant macroscopic optical SWIR SESAM parameters with respect to the design, MBE growth and strain relaxation. Antiresonant InGaSb QW SESAMs were designed for an operation wavelength from 2–2.4 µm to obtain low saturation fluence and broadband operation. We have identified the effects of strain, strain relaxation, QW number, and QW type (type-I or type-II), and barrier material on absorption properties and recovery dynamics of these SESAMs. This clearly confirmed earlier results [29], namely that Auger recombination is the dominant mechanism to obtain a fast SESAM without defect engineering in this material system. This can be considered a clear advantage for fast saturable absorber applications. Depending on applications the interband recombination time can be adjusted by using the quaternary $Al_xGa_{1-x}AsSb$ barrier material. This can become useful for self-starting passive modelocking.

For the 2–µm type-I SESAMs, we still have obtained $In_xGa_{1-x}Sb$ QWs with strained high crystal quality grown on top of a GaSb/ $AlAs_{0.08}Sb_{0.92}$ DBR with 20 pairs with a thickness of 5.8 µm. These 2-µm SESAMs are suitable for passively modelocked diode-pumped ion-doped solid-state and semiconductor lasers which has been confirmed experimentally [11,35,47].

For the 2.35-µm type-I SESAMs, the In content and the thickness of the $In_xGa_{1-x}Sb$ QWs have crossed the critical thickness such that strain relaxation took place during the MBE growth. This increased the nonsaturable losses which however can be reduced to below 10% of ΔR when choosing $AlAs_{0.08}Sb_{0.92}$ as barrier material in the absorber section. However, the final outcome becomes more critical on the exact growth parameters and the $F_{sat}\Delta R$ product shows larger fluctuations, possibly explained by additional defect-related scattering centers. The final 2.35-µm SESAM parameters were still sufficiently good to obtain record performance from SESAM modelocked diode-pumped solid-state laser [11,33].

Even though strain relaxation induced defect centers exist in the crystal, Auger recombination is the dominant nonradiative recombination process due to high carrier confinement and large Auger coefficients for small bandgap materials. In addition, low nonsaturable losses of a strained-relaxed SESAM makes it possible to be used in high-Q laser cavities. All type-I SESAMs show excellent

Optical Materials EXPRESS

performance, which is suitable for modelocking of diode-pumped semiconductor, solid-state, and thin-disk lasers. The dependence of the SESAM design, i.e., QW number, the barrier material and the design wavelength on saturation parameters is investigated. SESAMs for different wavelengths are successfully bandgap engineered without the need of quaternary materials or strain compensation. For the first time a detailed characterization has been used to investigate SESAMs at different wavelengths in the SWIR. Further improvements for femtosecond pulse generation will focus on lattice-matched, quaternary InGaAsSb QWs and a DBR material that minimizes ISA by avoiding two-photon absorption in GaSb [48,49].

Future work is focused on the demonstration of modelocked integrated external cavity surface emitting lasers (MIXSELs) [50,51], for which the gain and absorber layers are integrated into one wafer structure. Based on this work we can consider for an operation wavelength around 2 µm a type-I GaSb-based MIXSEL chip. We have also demonstrated that a type-II W-like AlSb/InAs/GaSb/InAs/AlSb SESAM can generate sufficient modulation depth by scaling the number of W-like QWs to compensate for the lower wave function overlap in the recombination. This has increased the recovery time into the nanosecond regime because the lower wave function overlap substantially reduces the Auger recombination. For SESAM applications the type-II W-like quantum well absorbers, however, is too slow for reliable passive modelocking and therefore these QW structures are more suited for active devices such as VECSELs and MIXSELs. We therefore will consider for longer wavelengths well beyond 2-µm a type-II QW-based gain and type-I QW-based saturable absorber for the MIXSEL chip design. Combined with dual-comb modelocking [52] this will open up the path towards molecular spectroscopy applications with extremely fast acquisition times as demonstrated with dual-comb MIXSELs in the near-infrared [53,54].

Funding. H2020 European Research Council (ERC advanced grant 787097 ONE-MIX).

Acknowledgements. We thank FIRST clean room facility at ETH Zurich.

Disclosures. The authors declare that there are no conflicts of interest related to this article.

Data availability. Data underlying the results presented in this paper are not publicly available at this time but may be obtained from the authors upon reasonable request.

References

1. U. Keller, K. J. Weingarten, F. X. Kärtner, D. Kopf, B. Braun, I. D. Jung, R. Fluck, C. Hönninger, N. Matuschek, and J. Aus Der Au, "Semiconductor saturable absorber mirrors (SESAM's) for femtosecond to nanosecond pulse generation in solid-state lasers," IEEE J. Sel. Top. Quantum Electron. **2**(3), 435–453 (1996).
2. C. Hönninger, R. Paschotta, F. Morier-Genoud, M. Moser, and U. Keller, "Q-switching stability limits of continuous-wave passive mode locking," J. Opt. Soc. Am. B **16**(1), 46 (1999).
3. I. D. Jung, F. X. Kärtner, N. Matuschek, D. H. Sutter, F. Morier-Genoud, Z. Shi, V. Scheuer, M. Tilsch, T. Tschudi, and U. Keller, "Semiconductor saturable absorber mirrors supporting sub-10-fs pulses," Appl. Phys. B: Lasers Opt. **65**(2), 137–150 (1997).
4. F. Saltarelli, I. J. Graumann, L. Lang, D. Bauer, C. R. Phillips, and U. Keller, "Power scaling of ultrafast oscillators: 350-W average-power sub-picosecond thin-disk laser," Opt. Express **27**(22), 31465 (2019).
5. R. Paschotta, L. Krainer, S. Lecomte, G. J. Spühler, S. C. Zeller, A. Aschwanden, D. Lorenser, H. J. Unold, K. J. Weingarten, and U. Keller, "Picosecond pulse sources with multi-GHz repetition rates and high output power," New J. Phys. **6**(1), 174 (2004).
6. A. E. H. Oehler, M. C. Stumpf, S. Pekarek, T. Südmeyer, K. J. Weingarten, and U. Keller, "Picosecond diode-pumped 1.5 µm Er,Yb:glass lasers operating at 10-100 GHz repetition rate," Appl. Phys. B: Lasers Opt. **99**(1-2), 53–62 (2010).
7. A. Härkönen, C. Grebing, J. Paajaste, R. Koskinen, J. P. Alanko, S. Suomalainen, G. Steinmeyer, and M. Guina, "Modelocked GaSb disk laser producing 384fs pulses at 2 µm wavelength," Electron. Lett. **47**(7), 454–456 (2011).
8. M. Guina, A. Härkönen, J. Paajaste, J.-P. Alanko, S. Suomalainen, C. Grebing, and G. Steinmeyer, "Passively mode-locked GaSb-based VECSELs emitting sub-400-fs pulses at 2 µm," in *Vertical External Cavity Surface Emitting Lasers (VECSELs) II*, A. C. Tropper, ed. (SPIE, 2012), **8242**, p. 824204.
9. A. Härkönen, J. Paajaste, S. Suomalainen, J.-P. Alanko, C. Grebing, R. Koskinen, G. Steinmeyer, and M. Guina, "Picosecond passively mode-locked GaSb-based semiconductor disk laser operating at 2µm," Opt. Lett. **35**(24), 4090 (2010).

Optical Materials EXPRESS

10. S. Kivistö, T. Hakulinen, M. Guina, K. Rößner, A. Forchel, and O. Okhotnikov, “2 watt 2 μm Tm/Ho fiber laser system passively Q-switched by antimonide semiconductor saturable absorber,” in *Solid State Lasers and Amplifiers III*, J. A. Terry, T. Graf, and H. Jelínková, eds. (SPIE, 2008), **6998**, p. 69980Q.
11. A. Barh, J. Heidrich, B. O. Alaydin, M. Gaulke, M. Golling, C. R. Phillips, and U. Keller, “Watt-level and sub-100-fs self-starting mode-locked 2.4-μm Cr:ZnS oscillator enabled by GaSb-SESAMs,” Opt. Express **29**(4), 5934 (2021).
12. C. R. Pollock, N. A. Brilliant, D. Gwin, T. J. Carrig, W. J. Alford, J. B. Heroux, W. I. Wang, I. Vurgaftman, and J. R. Meyer, “Mode locked and q-switched Cr: ZnSe laser using a semiconductor saturable absorbing mirror (SESAM),” in *Optics InfoBase Conference Papers* (Optical Society of America (OSA), 2005), p. TuA6.
13. R. Koskinen, S. Suomalainen, J. Paajaste, S. Kivistö, M. Guina, O. Okhotnikov, and M. Pessa, “Highly nonlinear GaSb-based saturable absorber mirrors,” Nonlinear Optics and Applications III **7354**(May 2009), 73540G (2009).
14. J. Paajaste, S. Suomalainen, A. Harkonen, U. Griebner, G. Steinmeyer, and M. Guina, “Control of the absorption recovery time in GaSb SESAMs,” *2013 Conference on Lasers and Electro-Optics Europe and International Quantum Electronics Conference*, CLEO/Europe-IQEC 2013 19349(2012), 33101 (2013).
15. J. Paajaste, S. Suomalainen, A. Härkönen, U. Griebner, G. Steinmeyer, and M. Guina, “Absorption recovery dynamics in 2 m GaSb-based SESAMs,” J. Phys. D: Appl. Phys. **47**(6), 065102 (2014).
16. J. Heidrich, M. Gaulke, B. O. Alaydin, M. Golling, A. Barh, and U. Keller, “Full optical SESAM characterization methods in the 1.9 to 3-μm wavelength regime,” Opt. Express **29**(5), 6647 (2021).
17. J. Paajaste, S. Suomalainen, R. Koskinen, A. Härkönen, G. Steinmeyer, and M. Guina, “GaSb-based semiconductor saturable absorber mirrors for mode-locking 2 μm semiconductor disk lasers,” Phys. Status Solidi C **9**(2), 294–297 (2012).
18. F. X. Kärtner, I. D. Jung, and U. Keller, “Soliton mode-locking with saturable absorbers,” IEEE J. Sel. Top. Quantum Electron. **2**(3), 540–556 (1996).
19. U. Keller, T. H. Chiu, and J. F. Ferguson, “Self-starting femtosecond mode-locked Nd:glass laser that uses intracavity saturable absorbers,” Opt. Lett. **18**(13), 1077 (1993).
20. U. Siegner, M. Haiml, F. Morier-Genoud, R. C. Lutz, P. Specht, E. R. Weber, and U. Keller, “Femtosecond nonlinear optics of low-temperature grown semiconductors,” Phys. B (Amsterdam, Neth.) **273-274**, 733–736 (1999).
21. H. H. Tan, C. Jagadish, M. J. Lederer, B. Luther-Davies, J. Zou, D. J. H. Cockayne, M. Haiml, U. Siegner, and U. Keller, “Role of implantation-induced defects on the response time of semiconductor saturable absorbers,” Appl. Phys. Lett. **75**(10), 1437–1439 (1999).
22. M. J. Lederer, B. Luther-Davies, H. H. Tan, C. Jagadish, M. Haiml, U. Siegner, and U. Keller, “Nonlinear optical absorption and temporal response of arsenic- and oxygen-implanted GaAs,” Appl. Phys. Lett. **74**(14), 1993–1995 (1999).
23. M. Mangold, V. J. Wittwer, C. A. Zaugg, S. M. Link, M. Golling, B. W. Tilma, and U. Keller, “Femtosecond pulses from a modelocked integrated external-cavity surface emitting laser (MIXSEL),” Opt. Express **21**(21), 24904 (2013).
24. C. J. Saraceno, C. Schriber, M. Mangold, M. Hoffmann, O. H. Heckl, C. R. E. Baer, M. Golling, T. Südmeyer, and U. Keller, “SESAMs for high-power oscillators: Design guidelines and damage thresholds,” IEEE J. Sel. Top. Quantum Electron. **18**(1), 29–41 (2012).
25. X. Liu, A. Prasad, W. M. Chen, A. Kurpiewski, A. Stoschek, Z. Liliental-Weber, and E. R. Weber, “Mechanism responsible for the semi-insulating properties of low-temperature-grown GaAs,” Appl. Phys. Lett. **65**(23), 3002–3004 (1994).
26. M. Haiml, U. Siegner, F. Morier-Genoud, U. Keller, M. Luysberg, R. C. Lutz, P. Specht, and E. R. Weber, “Optical nonlinearity in low-temperature-grown GaAs: Microscopic limitations and optimization strategies,” Appl. Phys. Lett. **74**(21), 3134–3136 (1999).
27. M. Haiml, U. Siegner, F. Morier-Genoud, U. Keller, M. Luysberg, P. Specht, and E. R. Weber, “Femtosecond response times and high optical nonlinearity in beryllium-doped low-temperature grown GaAs,” Appl. Phys. Lett. **74**(9), 1269–1271 (1999).
28. T. Finke, J. Nürnberg, V. Sichkovskyi, M. Golling, U. Keller, and J. P. Reithmaier, “Temperature resistant fast In_xGa_{1-x}/GaAs quantum dot saturable absorber for the epitaxial integration into semiconductor surface emitting lasers,” Opt. Express **28**(14), 20954 (2020).
29. K. S. Gadedjisso-Tossou, S. Belahsene, M. A. Mohou, E. Tournié, and Y. Rouillard, “Recombination channels in 2.4-3.2 μm GaInAsSb quantum-well lasers,” Semicond. Sci. Technol. **28**(1), 015015 (2013).
30. B. Rösener, M. Rattunde, R. Moser, S. Kaspar, C. Manz, K. Köhler, and J. Wagner, “GaSb-based optically pumped semiconductor disk lasers emitting in the 2.0-2.8 μm wavelength range,” in *Solid State Lasers XIX: Technology and Devices*, W. A. Clarkson, N. Hodgson, and R. K. Shori, eds. (SPIE, 2010), 7578, p. 75780X.
31. B. Rösener, M. Rattunde, R. Moser, S. Kaspar, T. Töpper, C. Manz, K. Köhler, and J. Wagner, “Continuous-wave room-temperature operation of a 2.8 μm GaSb-based semiconductor disk laser,” Opt. Lett. **36**(3), 319 (2011).
32. D. J. H. C. Maas, A. R. Bellancourt, M. Hoffmann, B. Rudin, Y. Barbarin, M. Golling, T. Südmeyer, and U. Keller, “Growth parameter optimization for fast quantum dot SESAMs,” Opt. Express **16**(23), 18646 (2008).
33. A. Barh, BÖ Alaydin, J. Heidrich, M. Gaulke, M. Golling, C. R. Phillips, and U. Keller, “High-power low-noise 2-GHz femtosecond laser oscillator at 2.4 μm,” Opt. Express **30**(4), 5019 (2022).
34. M. Kuznetsov, F. Hakimi, R. Sprague, and A. Mooradian, “High-power (>0.5-W CW) diode-pumped vertical-external-cavity surface-emitting semiconductor lasers with circular TEM 00 beams,” IEEE Photon. Technol. Lett. **9**(8), 1063–1065 (1997).

Optical Materials EXPRESS

35. J. Heidrich, M. Gaulke, M. Golling, B. O. Alaydin, A. Barh, and U. Keller, "324-fs Pulses From a SESAM Modelocked Backside-Cooled 2-µm VECSEL," IEEE Photon. Technol. Lett. **34**(6), 337–340 (2022).
36. M. Yano, Y. Kazuhiko, U. Takashige, and M. Inoue, "Reflection high-energy electron diffraction study of the GaSb surface during molecular beam epitaxy," J. Vac. Sci. Technol., B: Microelectron. Process. Phenom. **12**(2), 1133 (1994).
37. A. S. Bracker, M. J. Yang, B. R. Bennett, J. C. Culbertson, and W. J. Moore, "Surface reconstruction phase diagrams for InAs, AlSb, and GaSb," J. Cryst. Growth **220**(4), 384–392 (2000).
38. M. Gaulke, J. Heidrich, B. Özgür Alaydin, M. Golling, A. Barh, and U. Keller, "High average output power from a backside-cooled 2-µm InGaSb VECSEL with full gain characterization," Opt. Express **29**(24), 40360 (2021).
39. S. J. Maddox, S. D. March, and S. R. Bank, "Broadly tunable AlInAsSb digital alloys grown on GaSb," Crys. Growth Des. **16**(7), 3582–3586 (2016).
40. S. Birner, T. Zibold, T. Andlauer, T. Kubis, M. Sabathil, A. Trellakis, and P. Vogl, "Nextnano: general purpose 3-D simulations," IEEE Trans. Electron Devices **54**(9), 2137–2142 (2007).
41. J. R. Meyer, C. A. Hoffman, F. J. Bartoli, and L. R. Ram-Mohan, "Type-II quantum-well lasers for the mid-wavelength infrared," Appl. Phys. Lett. **67**(6), 757–759 (1995).
42. G. J. Spühler, K. J. Weingarten, R. Grange, L. Krainer, M. Haiml, V. Liverini, M. Golling, S. Schön, and U. Keller, "Semiconductor saturable absorber mirror structures with low saturation fluence," Appl. Phys. B: Lasers Opt. **81**(1), 27–32 (2005).
43. T. A. Nilsen, M. Breivik, E. Selvig, and B. O. Fimland, "Critical thickness of MBE-grown Ga1-xInxSb (x<0.2) on GaSb," J. Cryst. Growth **311**(7), 1688–1691 (2009).
44. R. Grange, M. Haiml, R. Paschotta, G. J. Spühler, L. Krainer, M. Golling, O. Ostinelli, and U. Keller, "New regime of inverse saturable absorption for self-stabilizing passively mode-locked lasers," Appl. Phys. B: Lasers Opt. **80**(2), 151–158 (2005).
45. U. Keller, "Ultrafast all-solid-state laser technology," Appl. Phys. B: Lasers Opt. **58**(5), 347–363 (1994).
46. S. Tomilov, Y. Wang, M. Hoffmann, J. Heidrich, M. Golling, U. Keller, and J. C. Saraceno, "50-W average power SESAM-modelocked thin-disk oscillator at 2.1 µm," in preperation for Optics Express (n.d.).
47. S. Tomilov, M. Hoffmann, J. Heidrich, B. O. Alaydin, M. Golling, Y. Wang, U. Keller, and C. J. Saraceno, "40 W SESAM-modelocked Ho:YAG thin-disk laser at 2090nm," in *2021 Conference on Lasers and Electro-Optics Europe and European Quantum Electronics Conference*, CLEO/Europe-EQEC 2021 (Institute of Electrical and Electronics Engineers Inc., 2021).
48. M. D. Turner, W. B. Roh, and K. L. Schepler, "Nonlinear optical properties of GaSb and GaInAsSb and their application for phase conjugation in degenerate four-wave mixing," J. Opt. Soc. Am. B **17**(5), 790 (2000).
49. E. W. van Stryland, M. A. Woodall, H. Vanherzeele, and M. J. Soileau, "Energy band-gap dependence of two-photon absorption," Opt. Lett. **10**(10), 490 (1985).
50. B. W. Tilma, M. Mangold, C. A. Zaugg, S. M. Link, D. Waldburger, A. Klenner, A. S. Mayer, E. Gini, M. Golling, and U. Keller, "Recent advances in ultrafast semiconductor disk lasers," Light: Sci. Appl. **4**(7), e310 (2015).
51. D. J. H. C. Maas, A. R. Bellancourt, B. Rudin, M. Golling, H. J. Unold, T. Südmeyer, and U. Keller, "Vertical integration of ultrafast semiconductor lasers," Appl. Phys. B: Lasers Opt. **88**(4), 493–497 (2007).
52. S. M. Link, A. Klenner, M. Mangold, M. Golling, B. W. Tilma, and U. Keller, "Dual-comb modelocked lasers," Opt. Express **23**(5), 5521–5531 (2015).
53. S. M. Link, D. J. H. C. Maas, D. Waldburger, and U. Keller, "Dual-comb spectroscopy of water vapor with a free-running semiconductor disk laser," Science **356**(6343), 1164–1168 (2017).
54. J. Nürnberg, C. G. E. Alfieri, Z. Chen, D. Waldburger, N. Picqué, and U. Keller, "An unstabilized femtosecond semiconductor laser for dual-comb spectroscopy of acetylene," Opt. Express **27**(3), 3190 (2019).